Phys. Med. Biol. **41** (1996) 1227–1232. Printed in the UK

The inversion of the exponential Radon transform for quantitative brain SPECT

Zhengrong Liang, Jinghan Ye, Juihsi Cheng and Donald P Harrington
Department of Radiology, State University of New York, Stony Brook, NY 11794, USA

Received 11 August 1995, in final form 23 February 1996

Abstract. The mathematical derivation for the inversion of the exponential Radon transform is presented and the implementation of the inversion is detailed. The inversion can be verified and implemented by the readers for practical applications, such as for quantitative reconstruction of brain SPECT (single-photon emission computed tomography).

1. Introduction

In our previous paper (Liang *et al* 1994), we briefly outlined a procedure for the inversion of the exponential Radon transform or the line integral, based on the work of Inouye *et al* (1989),

$$p(\xi, \theta, \mu) = \int_{-\infty}^{\infty} \mathrm{d}\eta \, o(x, y) \mathrm{e}^{-\mu\eta} \tag{1}$$

where $o(x, y)$ represents the source distribution in the stationary coordinates (x, y), (ξ, η) stands for the rotation coordinates, μ is a known constant associated with the media in which the source is distributed, and θ is the rotation angle between ξ-axis and x-axis. In the paper, we did not provide all the mathematical formulas for the inversion and did not describe the implementation of the inversion on a digital computer. The lack of detailed derivation and implementation may cause difficulty for the readers in verifying the inversion and coding the mathematical formulas into computer programs for applications. In this note, we present the detailed derivation and implementation, so the procedure of the inversion can be performed by the readers for application.

2. Theory

The integral transform of (1) has a potential application in quantitative brain SPECT (single-photon emission computed tomography), where $p(\xi, \theta, \mu)$ is the measured number of primary photons, at projection angle θ, which are emitted from the radiotracer distribution $o(x, y)$ inside the brain tissues, and μ is the linear attenuation coefficient of those tissues. The goal is to find $o(x, y)$ from the measured data $p(\xi, \theta, \mu)$.

By a Fourier transform (FT) on the variable ξ for both sides of (1), we have

$$P(\omega, \theta, \mu) = O[\omega, \cos(\theta) + \mathrm{i}\mu \sin(\theta), \omega \sin(\theta) - \mathrm{i}\mu \cos(\theta)] \tag{2}$$

0031-9155/96/071227+06$19.50 © 1996 IOP Publishing Ltd

where $P(\omega, \theta, \mu)$ represents the one-dimensional (1D) FT of $p(\xi, \theta, \mu)$ on the spatial variable ξ (ω is the spatial frequency), and $O(\omega, \theta)$ stands for the 2D FT of $o(x, y)$. By employing the definition of Inouye *et al* (1989)

$$\omega = \rho \cos(\beta) \qquad -\mathrm{i}\mu = \rho \sin(\beta) \tag{3}$$

and using the relation $\exp(\mathrm{i}\beta) = \cos(\beta) + \mathrm{i}\sin(\beta) = (\omega/\rho) + \mathrm{i}(-\mathrm{i}\mu/\rho)$, we have

$$\beta = \mathrm{i}\ln[\rho/(\omega + \mu)]. \tag{4}$$

If only the positive values $\rho = \sqrt{\omega^2 - \mu^2}$ are selected, (2)–(4) resemble the inverse equation of Bellini *et al* (1979, (4)). Since both $P(\omega, \theta, \mu)$ and $O(\omega, \theta)$ are periodic functions of θ, a Fourier series expansion on these functions, via (2), gives

$$O_n(\rho) = P_n(\omega, \mu)\mathrm{e}^{-\mathrm{i}n\beta} = P_n(\omega, \mu)\left(\frac{\rho}{\omega + \mu}\right)^n \tag{5}$$

where

$$P_n(\omega, \mu) = \frac{1}{2\pi}\int_0^{2\pi} \mathrm{d}\theta\, P(\omega, \theta, \mu)\mathrm{e}^{-\mathrm{i}n\theta} \tag{6}$$

and a similar definition for $O_n(\rho)$. Based on the selection of $\rho = \sqrt{\omega^2 - \mu^2}$, the inverse (5) for the exponential Radon transform has been derived by Tretiak and Metz (1980, (33), (34)), Hawkins *et al* (1988, (25)), and Inouye *et al* (1989, (13)). Because only the positive values, $\rho \geqslant 0$, are selected, there are infinite combinations of $P_n(\omega < 0, \mu)$ and $P_n(\omega > 0, \mu)$ to determine $O_n(\rho)$ (Metz and Pan 1995). In this note, we show an one-to-one mapping between $O_n(\rho)$ and $P_n(\omega, \mu)$, $-\infty < \rho < \infty$ and $-\infty < \omega < \infty$.

In SPECT application, since both ω and μ are real valued, and ρ should be also real, then, from (4), β is an imaginary variable. Let $\beta = \mathrm{i}\alpha$, where α is a real variable, and from (3), we have

$$\omega = \rho\cos(\mathrm{i}\alpha) = (\rho/2)(\mathrm{e}^{\alpha} + \mathrm{e}^{-\alpha}) \qquad \mu = \mathrm{i}\rho\sin(\mathrm{i}\alpha) = (\rho/2)(\mathrm{e}^{-\alpha} - \mathrm{e}^{\alpha}) \tag{7}$$

i.e. (ω, μ) and (ρ, α) have an one-to-one mapping relation and all are real valued. It is noted that ω and ρ have the same sign. If $\omega \geqslant 0$, $\rho \geqslant 0$, while if $\omega < 0$, $\rho < 0$. This is very important for a unique implementation of the inversion of (5). Since $\omega + \mu = \rho\exp(-\alpha)$ and $\omega - \mu = \rho\exp(\alpha)$ by (7), $|\omega| \geqslant \mu$ is required. By the relation $\omega^2 + (\mathrm{i}\mu)^2 = \omega^2 - \mu^2 = \rho^2$, we have

$$\rho(\omega) = \begin{cases} +\sqrt{\omega^2 - \mu^2} & \text{if } \omega \geqslant \mu \\ -\sqrt{\omega^2 - \mu^2} & \text{if } \omega < -\mu \end{cases} \qquad \omega(\rho) = \begin{cases} +\sqrt{\rho^2 + \mu^2} & \text{if } \rho \geqslant 0 \\ -\sqrt{\rho^2 + \mu^2} & \text{if } \rho < 0. \end{cases} \tag{8}$$

The implementation of (5) is then uniquely determined by the mapping from coordinates ω–n of $P_n(\omega, \mu)$ to coordinates ρ–n of $O_n(\rho)$.

3. Implementation

Implementation of the inversion equations (5) and (8) on a digital computer is not trivial. A straightforward approach starts by computing $P_n(\omega, \mu)$ using a FT on $p(\xi, \theta, \mu)$ and (6), where ω and θ can be uniformly divided by the number of samples equal to the power of two, so a 2D fast FT (FFT) can be applied. Then the approach determines $O_n(\rho)$ by (5) and (8). Since ω is uniformly divided, the values of ρ determined by (8) will not be uniformly sampled. So an interpolation of complex-valued function $O_n(\rho)$ in the Fourier space is

required (Bellini *et al* 1979, Inouye *et al* 1989, Metz and Pan 1995). The interpolation can cause significant errors, especially for high-frequency components, where the sharp edge and noise play an important role.

In order to avoid the frequency-space interpolation, we start by selecting $\rho = \pm 0.5, \pm 1.5, \pm 2.5, \ldots$ to determine the corresponding values $\omega = \pm\sqrt{\rho^2 + \mu^2}$, and then compute the values of $P_n(\omega, \mu)$ by (6). Since ω is not uniformly sampled when ρ is uniformly divided, an ordinary FT is used for $P(\omega, \theta, \mu)$, instead of an FFT. An FFT is used for (6) on the angular variable θ. The reasons for the shift of ρ from the start point of zero to ± 0.5 are (i) to avoid the singular points of $\omega \pm \mu = 0$, (ii) to preserve the sampling symmetry of $O_n(\rho)$ for positive and negative values of ρ on a uniform increment, and (iii) to optimize the condition $|\omega| > \mu$. After $O_n(\rho)$ is obtained from $P_n(\omega, \mu)$ by (5) and (8), an inverse FFT is applied for the angular variable ϕ to compute the attenuation-compensated projection $P(\rho, \phi, \mu = 0)$ by

$$P(\rho, \phi, \mu = 0) = \sum_{n=-\infty}^{\infty} O_n(\rho) e^{in\phi} = \int_{-\infty}^{\infty} d\lambda \, O(\rho, \lambda) e^{i\lambda\phi} \tag{9}$$

where ϕ is defined by $0 \leqslant \phi < 2\pi$ and the summation on index n is replaced by the integral over λ. Finally, $P(\rho, \phi, \mu = 0)$ is filtered (by the Ramp filter with a low-pass window), inverse Fourier transformed (by an ordinary FT), and backprojected for each angle ϕ to reconstruct the source distribution $o(x, y)$.

In order to minimize the computing time, the following symmetrical properties are considered. From (2), there is

$$P(-\omega, \theta, \mu) = P^*(\omega, \theta, \mu). \tag{10}$$

This property would save half time when computing the FT of the measured data $p(\xi, \theta, \mu)$ on the spatial variable ξ. By (6) and (10), we have

$$P_{-n}(-\omega, \mu) = P_n^*(\omega, \mu) \qquad P_{-n}(\omega, \mu) = P_n^*(-\omega, \mu). \tag{11}$$

This property would again cut off half computing time when (6) is used for FFT on the angular variable θ.

The symmetrical property of the attenuation compensation filter $f(\omega, n) = \chi^n(\omega)$, with $\chi(\omega) = \rho/(\omega + \mu)$, is useful in reducing the computing time for $O_n(\rho)$ via (5),

$$f(-\omega, -n) = f(\omega, n) \qquad f(\omega, -n) = f(-\omega, n). \tag{12}$$

From (11) and (12), we have

$$O_{-n}(-\rho) = O_n^*(\rho) \qquad O_{-n}(\rho) = O_n^*(-\rho) \tag{13}$$

i.e. we only need to compute $O_n(\rho)$ in two quadrants: the first quadrant ($\rho \geqslant 0, n \geqslant 0$) and the second one ($\rho < 0, n \geqslant 0$), in the ρ–n plane, or in the ω–n plane ($\omega \geqslant 0, n \geqslant 0$) and ($\omega < 0, n \geqslant 0$). The values of $O_n(\rho)$ in the third quadrant ($\rho < 0, n < 0$) can be deduced from the values in the first quadrant and the values in the fourth quadrant ($\rho \geqslant 0, n < 0$) can be obtained from those of the second quadrant. The inversion with these symmetrical properties can be described graphically as follows.

On the left of figure 1 is shown the amplitude $|P_n(\omega, \mu)|$ in the ω–n plane, where ω is the horizontal axis and n is the vertical axis. These FT coefficients are computed from a noise-free sinogram $p(\xi, \theta, \mu)$ simulated by projecting a phantom in parallel-beam geometry at 128 equally spaced views on 360°. Each view has 128 equally spaced bins. The phantom (on an array of 128×128) consists of two small circular sources (radius of 3 pixels) inside a uniform (water) attenuating medium (a circle of radius of 32 pixels). These two small sources with centres on the x-axis are located on

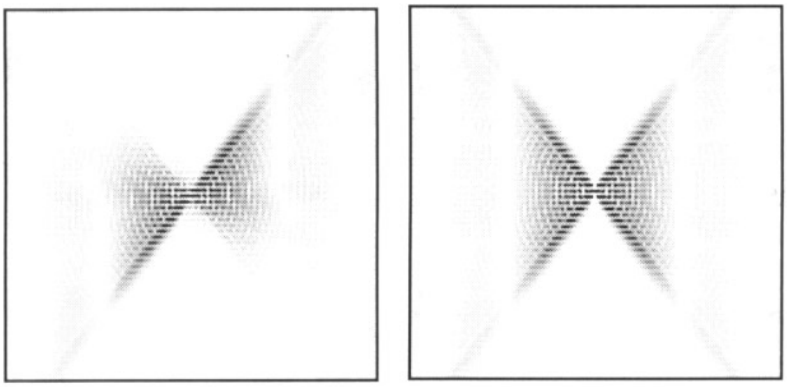

Figure 1. Two-dimensional FT coefficients $|P_n(\omega, \mu)|$ of a noise-free sinogram in the ω–n plane, where ω is the spatial frequency (on the horizontal axis) and n is the angular frequency (on the vertical axis). On the left is the FT of the attenuated sinogram, and on the right is that of the attenuation-free one.

both sides of the origin at an equal distance of 15 pixels from the y-axis. The values of $P_n(\omega, \mu)$ in the first and third quadrants reflect the contributions mainly from the sources located within the distance (equal to the radius of rotation) toward the collimator at all views, i.e. they are the near-field contributions, as described by Edholm *et al* (1986). The values in the second and fourth quadrants are the far-field contributions, which are attenuated much more than those of near-field contributions. As compared to the attenuation-free FT coefficients, (as shown on the right, which has the symmetry in all four quadrants and is computed from the same circular phantom), the inversion is to modify the $P_n(\omega, \mu)$ values in the first and second quadrants by the attenuation-compensation filter $f(\omega, n)$, and then to determine others in the third and fourth quadrants by the symmetries of (13). The modification will increase the values of the second quadrant and may decrease the values of the first quadrant in order to achieve the symmetry in all quadrants, as the attenuation-free one has. It is noted that in the noise- and attenuation-free (or attenuation compensated) case $O_n(-\rho) = (-1)^n O_n(\rho)$. This is because of the redundancy of projections from 180 to 360°, as compared to those projections from 0 to 180°. However, in the noisy case, this redundancy no longer exists.

In the first quadrant, since $\chi(\omega) < 1$, $f(\omega, n) = \chi^n(\omega)$ decreases as n increases, so the modification for $O_n(\rho) = P_n(\omega, \mu) f(\omega, n)$ is stable or convergent when implementation is performed by a digital computer. However, in the second quadrant, since $\chi(\omega) > 1$, $f(\omega, n)$ increases rapidly following n and diverges for small values of $|\omega|$. In order to avoid the divergence, $P_n(\omega, \mu)$ must go to zero at the same rate as $f(\omega, n)$ diverges, so the modification for $O_n(\rho)$ is stable. This is not the case, as shown on the left of figure 1. In the near-zero fields of $P_n(\omega, \mu)$ (i.e. the two triangular areas centred on the n-axis), $P_n(\omega, \mu)$ values greater than 0.1 can be found even for $|n| > 30$. To avoid this divergence, the $O_n(\rho)$ values in the near-zero fields are set to zero.

A flow chart for the implementation of the inversion on a digital computer is shown in figure 2, which details the conversion steps from the measured projection data $p(\xi, \theta, \mu)$ to the attenuation-compensated projections $p(\xi, \phi, \mu = 0)$.

```
[Perform ordinary Fourier transform in ξ dimension]
for ρ = 0.5 to N/2-0.5, stepsize 1.0
        ω = sqrt(ρ ρ + μ μ); [ω > 0]
        P(ω,θ,μ) = 0.0;  [P() is a complex matrix, and so is O()]
        for ξ  = -N/2 + 0.5 to N/2 - 0.5, stepsize 1.0
                P(ω,θ,μ) = P(ω,θ,μ) + p(ξ,θ,μ) exp(-i2πωξ/N);
        repeat;
        [Assign P(-ω,θ,μ) using symmetry property]
        P(-ω,θ,μ) = P*(ω,θ,μ);
repeat;

[Perform FFT in angular dimension]
P(ω,n,μ) = FFT(P(ω,θ,μ),θ);

[Scaling P(ω,n,μ)]
for ρ = 0.5 to N/2-0.5, stepsize 1.0
        ω = sqrt(ρ ρ + μ μ);
        b = ρ/(ω + μ);
        sign = -1;
        for n = 1 to N/2 - 1, stepsize 1
                scale = power(b, n);
                O(ρ,n) = P(ω,n,μ) scale;          [First quadrant]
                O(-ρ,n) = P(-ω,n,μ)/scale;       [Second quadrant]
                O(-ρ,-n) = O*(ρ,n);              [Third quadrant]
                O(ρ,-n) = O*(-ρ,n);              [Forth quadrant]
                sign = -sign;
        repeat;
repeat;

[Perform Inverse FFT in angular dimension]
P(ρ,ϕ,μ=0) = IFFT(O(ρ,n),n);

[Perform ordinary Inverse FT in ξ dimension]
for ξ = 0.5 to N/2-0.5, stepsize 1.0
        p(ξ,ϕ,μ=0) = 0.0;
        for ρ = -N/2 + 0.5 to N/2 - 0.5, stepsize 1.0
                p(ξ,ϕ,μ=0) = p(ξ,ϕ,μ=0) + P(ρ,ϕ,μ=0) exp(-i2πρξ/N);
        repeat;
repeat;

end.
```

Figure 2. Flow chart for attenuation compensation in the inversion of exponential Radon transform.

4. Conclusion

Inversion for the exponential Radon transform has potential application in quantitative brain SPECT. The above-presented procedure for the inversion is mathematically exact, and the implementation is computationally rigorous. The performance of the implementation described above is expected to be more robust, as compared to the straightforward approach mentioned, because the implementation avoids interpolation in frequency space. The cost of computing time, due to the use of the ordinary FT, rather than the FFT, is minimal (Liang *et al* 1994). A reconstruction of $128^2 \times 32$ image array from 128 projections takes less than 5 min on an HP/730 desktop computer.

Acknowledgment

This work was supported by grant No HL44194, awarded by the National Heart, Lung, and Blood Institute.

References

Bellini S, Piacentini M, Cafforio C and Rocca F 1979 Compensation of tissue absorption in emission tomography *IEEE Trans. Acoust. Speech Signal Processing* **ASSP-27** 213–18

Edholm P R, Lewitt R M and Lindholm B 1986 Novel properties of the fourier decomposition of the sinogram *Proc. SPIE* **671** 8–18

Hawkins W G, Leichner P K and Yang N C 1988 The circular harmonic transform for SPECT reconstruction and boundary conditions on the FT of the sinogram *IEEE Trans. Med. Imaging* **MI-7** 135–48

Inouye T, Kose K and Hasegawa A 1989 Image reconstruction algorithm for SPECT with uniform attenuation *Phys. Med. Biol.* **34** 299–304

Liang Z, Ye J and Harrington D P 1994 An analytical approach to quantitative reconstruction of non-uniform attenuated brain SPECT *Phys. Med. Biol.* **39** 2023–41

Metz C E and Pan X C 1995 A unified analysis of exact methods of inverting the 2D exponential Radon transform, with implications for noise control in SPECT *IEEE Trans. Med. Imaging* **MI-14** 643–58

Tretiak O and Metz C E 1980 The exponential Radon transform *SIAM J. Appl. Math.* **39** 341–54